Hassan and Fattah
Functional Composite Materials (2023) 4:1
https://doi.org/10.1186/s42252-023-00038-y

Functional Composite Materials

RESEARCH Open Access

Efficient removal of safranin from aqueous solution using a new type of metalated highly self-doped polyaniline nanocomposite

Hammed H. A. M. Hassan[1*] and Marwa Abdel Fattah[2]

Abstract

We report the chemical synthesis of poly(*aniline-co-aniline-2,5-disulfonic acid*)) and its composite containing L-hexuronic acid and metallic Ag/SiO_2 nanoparticles as a new thermally stable anionic polyelectrolyte for removing safranin dye. The composite was characterized by IR, UV, cyclic voltammetry, SEM, TEM, TGA, DSC, EDXS and elemental analyses. Microscopic images exhibited intensified spherical particles dispersed over almost the entire surface. The XRD exhibited peaks of the partially crystalline material at many 2θ values, and their interatomic spacing and sizes were calculated. The cyclic voltammograms exhibited characteristic redox peaks relative to the quinoid ring transition states. The uptake rates up to 82.5% adsorption were completed within 75 min and the equilibrium time was 45 min. The isotherm of dye adsorption interprets the interaction with the adsorbent and explain the relationship between the dye removal capacity and the initial dye concentration. In the current, the Langmuir isotherm model was the optimum to interpret both the dye/copolymer and the dye/composite interactions. The uptake of safranin by copolymer/SiO_2@Ag nanocomposite was well defined by pseudo second order model with rate constant $K_2 = 0.03\ g^{-1}\ mg^{-1}\ min^{-1}$ for 19 mg safranin. A comparison of safranin adsorption efficiency of the synthesized material with other reported material in the same domain suggested that the present composite has a higher adsorption rate and capacity. The ongoing research is devoted to improving the removal percentage of the dye by using 1,3,5-triazine based sulfonated polyaniline/Ag@ SiO_2 nanocomposite.

Keywords Adsorption, Dyes, Ag@SiO_2 nanocomposite, Sulfonated polyaniline, Safranin, Response surface

Introduction

Water pollution due to the dyeing of textile fibers, paper, leathers, plastics, and pharmaceuticals is one of the most challenging problems in industrial waste management because of its complexity, which directly influences drinking water [1, 2]. Some aromatic organic dyes are extremely hard-to-degrade and have toxic natures as exemplified by the cationic dye safranin; 3,7-diamino-2,8-dimethyl-5-phenylphenazinium chloride, Fig. 1 [3]. Several techniques have been applied to remove dyes and water pollutants from water as possible methods to avoid their side effect. These techniques include adsorption, advanced oxidation, filtration, coagulation, flocculation, and microbial degradation [4]. Photocatalytic degradation of safranin dye from water using mineral clay photocatalysts has been considered as a suitable and efficient method. Bentonite/polyaniline/Ni_2O_3 composite photocatalytic removal of safranin-O dye under sunlight exposure revealed better dye removal percentages than its individual components [5]. Natural zeolite heulandite/polyaniline composite displayed high stability and photocatalytic efficiency after 5 runs [6]. Polypyrrole

*Correspondence:
Hammed H. A. M. Hassan
hamed.hassan@alexu.edu.eg
[1] Chemistry Department, Faculty of Science, Alexandria University, P.O. 2, Moharram Beck, Alexandria, Egypt
[2] Menoufia Higher Institute of Engineering and Technology MNF-HIET, Menoufia, Egypt

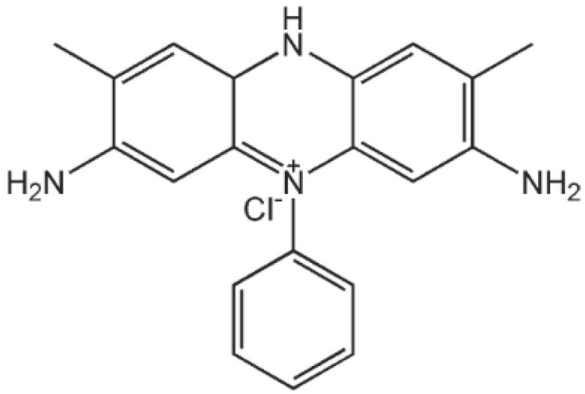

Fig. 1 Chemical structure of safranine

nanofiber/Zn-Fe layered double hydroxide was assessed as efficient safranin dye adsorbent. The adsorption of safranin by the composite occurred in a multilayer form and the complete photocatalytic removal of 5 mg/L of the dye achieved after 120 min illumination time using 0.05 g of the composite as photocatalyst and the best results can be obtained at neutral to alkaline conditions [4]. Among many approaches employed for the removal of dyestuff, the adsorption approach exhibits interesting advantages such as high efficiency, ease of use, low energy consumption, and cost-effectiveness [7]. Nevertheless, the reported shortcomings of the investigated adsorbents such as unacceptable reusability; and weak adsorption rate and capacity, highlight the need for new adsorbents with improved capabilities [8].

According to the literature reports, polymeric adsorbents exhibit a high surface area with pore size distribution, mechanical rigidity, and easy regeneration under mild conditions [9]. Polyaniline and its derivatives exhibit potent environmental stability and high adsorption capacities [10]. Polyaniline composites have often been used instead of neat polyaniline in the search for various application forms [11]. Polymeric composites with metal oxides improved adsorption sites, adsorption capacity, and surface area; and decreased the polymer-dye equilibrium time [12]. Notably, the poor conductivity of such polymers never disqualifies them as being good adsorbents. Polyaniline-silicon is a traditional adsorbent for rapidly removing many dyes such as amido black 10B, methylene blue or reactive orange 16 from aqueous solutions [13, 14]. Polyaniline/mesoporous silicate efficiently removed acid blue 62, acid violet 90, reactive red 2 and reactive blue 194 [15]. A polyaniline/silver nanocomposite, using the reductive properties of this conducting polymer on silver ions, was used for the adsorption of brilliant green [16]. Substituted polyanilines have been used in the adsorption of adsorbed anionic azo dyes, acid red 4, direct red 23 and reactive red 198 [15]. Polymerization of aniline derivatives containing sulfonic groups leads to self-doped polyaniline, which is independent of external protonation in a broad pH range [16]. The expected promising sulfonated polymer–dye interaction may open a new pathway to address such pollution threats [17]. Notably, dyes containing functionalities such as -OH, $-NH_2$, $-NR_2$, and $-SO_3H$ facilitate various interactions with the polyelectrolyte which may be electrostatic, hydrophilic/hydrophobic, H-bonding, covalent, or nonbonding.

As a part of an ongoing project directed to new findings in the field of water treatment using functionalized polyanilines as highly promising candidates [18, 19, 20, 21], we investigated the use of (aniline-co-aniline-2,5-disulfonic acid)/L-hexuronic acid/Ag@SiO_2 nanocomposites as a new highly anionic polyelectrolyte with an enhanced adsorptive effect for removing the cationic dye safranin. The incorporation of disulfonated units into the polymer chain should double the sulfonate groups on the backbone and produce regular molecular structure polymers with a higher sulfonation degree [22]. The silver-doped silica-complex spheres were prepared by the first hydrolysis of ethanol-diluted tetraethyl orthosilicate (TEOS) followed by the subsequent addition of silver nitrate and $NaBH_4$. The composite was characterized with IR, UV, XRD, cyclic voltammetry, scanning and transmission electron microscopy, thermogravimetric and differential scanning calorimetry measurements. The effects of experimental parameters such as pH, adsorbent dose, contact time, and dye concentration were investigated for safranin adsorption. To the best of our knowledge, no studies on the use of polyaniline derivatives/silica nanocomposites as adsorbents for the removal of heavy metal ions/dyes from aqueous solutions have been reported to date.

Experimental

Materials

Commercial aniline (AlGomhoria Chemicals Co.; Egypt), 2-aminobenzene-1,4-disulfonic acid (ICI, Manchester, UK), ammonium persulfate (Oxford Lab Fine Chemicals, India), and tetraethyl orthosilicate (TEOS) (98%, Sigma-Aldrich, Steinheim, Germany) were used. Silver nitrate (99.9%, HOLPRO ANALYTICS DIVISION, Midrand, INDIA), sodium borohydride (95%, Fluka, Switzerland), and ascorbic acid (99.7%, Riedel-De Haen AG, Seelze-Hannover). Ethanol and ammonia solution (30%) were used as purchased. All chemicals were used without further purification.

Measurements

Infrared spectra (IR, KBr pellets; 3 mm thickness) were recorded on a Perkin-Elmer Infrared Spectrophotometer (FTIR 1650). All spectra were recorded within the wavenumber range of 4000–600 cm^{-1} at 25 °C. Absorption spectra were measured with a UV 500 UV–Vis spectrometer at 16 °C (rt) in DMSO with a polymer concentration of 2 mg/10 mL. Elemental analysis of the as-synthesized copolymer was performed at the Microanalytical Unit, Cairo University. Inherent viscosities (η_{inh}) were measured at a concentration of 0.5 g/dL in H_2SO_4 at 30 °C by using an Ubbelohde viscometer. Thermogravimetric (TG) and differential thermogravimetric (DTG) analyses were carried out in the temperature range from 20 °C to 400 °C in a nitrogen atmosphere by a Shimadzu DTG 60H thermal analyser. The experimental conditions were platinum crucible, nitrogen atmosphere with a 30 mL/min flow rate and a heating rate of 10 C/min. Differential scanning calorimetry (DSC-TGA) analyses were carried out using SDT-Q600-V20.5-Build-15 at the microanalytical unit, Cairo University. Cyclic voltammetry was performed using an eDAQ system (www.eDAQ.com, Australia) consisting of an ER466 potentiostat connected to an e-corder that was inputted to eChem software (running on a PC using Microsoft Windows 10). The working electrode was a 3 mm diameter glassy carbon electrode; the reference electrode was Ag/AgCl; and the auxiliary electrode was a 0.25 mm diameter Pt wire. The applied potentials ranged from − 500 to + 500 mV, and the scan rate during one cycle was 100 mV s^{-1}. The volume of the voltammetric cell was approximately 15 ml. The polymer powder was pressed to form discs with diameters of 10 mm and thicknesses of 1 mm. Silver electrodes were deposited on both sides of the sample surface by thermal evaporation, and two copper wires were fixed on the sample using conducting silver paint. Energy-dispersive X-ray spectroscopy (EDXS) and the morphologies of the polymers were observed by scanning electron microscopy (SEM) (JEOL-JSMIT 200, Japan) and transmission electron microscopy (TEM) (JEOL-JTM-1400 plus, Japan) at the E-Microscope Unit, Faculty of Science, Alexandria University. The samples were sonicated in deionized water for 5 min, deposited onto carbon-coated copper mesh and allowed to air-dry before examination.

Preparation of silver-doped silica-complex nanocomposite 3

The synthesis of silver-doped silica-complex spheres is slightly modified from the reported method [23]. In a 100 mL round bottom flask, a mixture of EtOH (25 ml) and NH_4OH (40 mL, 30%) was magnetically stirred for 10 min. TEOS 1 (10 ml) dissolved in EtOH (20 ml) was slowly added and stirring was continued for 10 min. Then, TEOS 1 (5 ml) diluted in EtOH (5 ml) was added, and the mixture was magnetically stirred for an additional 3 h at rt. After that, silver nitrate (0.5 g, 2.94 mmol) dissolved in distilled water (10 mL) was added to the stirred solution. After 30 min., $NaBH_4$ (250 mg, 6.61 mmol) was subsequently added and stirring was continued for an additional 10 h. The mixture was centrifuged at 2000 rpm for 20 min., and nanoparticle 3 was collected as a brawn solid which was repeatedly washed with distilled water and acetone to remove the unreacted and undesired byproducts. The obtained nanosized solid 3 was dried in a vacuum oven at 80 °C for 24 h. IR (KBr, υ cm^{-1}): 3468, 3459, 3449, 3437, 1635, 1500, 1459, 1420, 1402, 1385, 1364, 1281, 1081, 798, 465. UV—Vis (λ_{max} nm): ~ 400 nm. EDXS elemental analysis: O, 35.57; Si, 15.87; Ag, 45.28; Cl, 0.16; Na, 0. XRD (2θ): 23.5°, 38.5°, 44.8°, 64.3°, and 77.2°.

Synthesis of (aniline-co-aniline-2,5-disulfonic acid) polymer 6

The titled compound **6** was prepared and characterized, Additional file 4: Supplementary 1.

Synthesis of poly (aniline-co-aniline-2,5-disulfonic acid)/L-hexuronic acid/Ag@SiO_2 nanocomposite 7

Silver doped silica 3 (1.0 g), aniline-2,5-disulfonic acid 4 (12.65 g, 0.05 mol), aniline 5 (2.00 g, 0.0215 mol, 15.8% weight of 1) and L-ascorbic acid (2.00 g, 0.011 mol, 15.8% weight of 1) were subsequently added to an aqueous 10% HCl (500 ml), and a solution of ammonium persulfate (15.0 g, 0.0657 mol) dissolved in water (50 ml) was subsequently added over a period of 30 min. The mixture was mechanically stirred for 24 h at rt., and the color change pattern observed during the polymerization from the light yellow to light green and then finally dark green-brawn precipitate was observed from t ¼ 0 to 24 h. Polymerization was stopped by the addition of methanol (50 ml). The resulting precipitate was subsequently washed with water (3x), aqueous 1 M HCl (1x), water (1x) and acetone (1x) to remove the unreacted starting materials and short oligomers. Finally, the precipitate was dried in a vacuum oven at 50 °C. Yield: 4.15 g. IR (cm^{-1}, u): 3480, 3468, 3400, 1640, 1609, 1586, 1570, 1493, 1405, 1385, 1303, 1235, 1145, 1018, 881, 819, 802, 707, 667, 632, 597, 563, 550, 540, 506, 454. UV–vis (λ_{max} nm): 245, 375, 640. Calc. for $C_{42}H_{46}N_6S_2O_{26}$: (1115); C, 45.24; H, 4.16; N, 7.54; S, 5.75 S/2 N ratio 0.38; Found: C, 46.03; H, 4.58; N, 7.99; S, 5.33; S/2 N ratio 0.33.

Batch adsorption studies

A stock solution of safranine dye (1000 ppm) was prepared by dissolving 1.0 g of dye in 1.0 L distilled water.

The working solutions were obtained by diluting the stock solution. Typically, different amounts of oligomer 3 and nanocomposite 7 were added to 100 mL solutions with different dye concentrations under shaking conditions (300 rpm) at 25 °C for a particular time. Before adsorption, the pH value of each dye solution was measured. Different pH values were studied that were adjusted by using NaOH and HCl solutions (0.1 mol / L). Then, the nanocomposite and liquid phases were separated via centrifugation. The concentration of safranine dye was measured with a UV–vis spectrophotometer (Analytik Jena SPECORD 250, Germany). Equations (1) and (2) were used to determine the adsorption capacity (q, mg/g) of 3 and 7 and the removal percentage (% R), respectively. Equilibrium isotherms and adsorption kinetics for safranine dye were obtained by performing batch adsorption studies.

$$q = \frac{(Co - Ce)V}{m} \quad (1)$$

$$\%R = \frac{(Co - Ct)\,x100}{Co} \quad (2)$$

where C_o is the initial dye concentration (ppm), C_e is the concentration of dye at equilibrium (ppm), C_t is the dye concentration at different times (ppm), m is the adsorbent dosage (mg) and V is the solution volume (L). All chemicals used in the experiments were of analytic reagent grade.

Parameters affecting adsorption experiments

Effect of pH value The influence of pH on the sorption process was investigated for safranin adsorption onto 6 and nanocomposites 7 by shaking 2 g / L of sorbent in conical flasks with varied pH values (3–11) at 25 °C and 100 rpm with 50 mL of initial aqueous safranin dye solution (30 ppm). Both HCl and NaOH were used to modify the pH, and the equilibration time was set at 75 min.

Effect of various concentration of safranin dye verses contact time Study the effect of adding a various concentration of *safranin dye* with contact time was examined for 100 ml solutions with 20, 30, 40, and 50 ppm concentrations and containing 2 g/L adsorbent dose of 6 and 7 for 80 mins.

Effect of adsorbent dose Effect of adsorbent dose on dye uptake was investigated with 1, 2, 3, and 4 g / L of 30 ppm aqueous safranin dye solution for 75 min.

Adsorption kinetics and isotherms studies Different kinetic models are used to analyze the experimental data of different concentrations of safranin dye (20, 30, 40, 50 ppm for 75 min, 25 °C, 2 g / L adsorbent dose) for copolymer 6 and nanocomposite 7 according to equations of pseudo first order and pseudo second order, discussed later in the results section. Also, Langmiur and Freuindish isotherm types were investigated for different concentrations of safranin dye for copolymer 6 and nanocomposite 7 according to its equations, discussed later in the results section.

Results and discussion

Preparation of poly (aniline-co-aniline-2,5-disulfonic acid)/L-hexuronic acid/Ag@SiO_2 nanocomposite 7

As shown in Fig. 2, the silver-doped silica-complex spheres Ag@$SiO_2$3 were prepared by hydrolysis of tetraethyl orthosilicate (TEOS) 1 in ethanolic ammonia followed by subsequent addition of silver nitrate and $NaBH_4$. The copolymer 6 was chemically prepared from commercial aniline-2,5-disulfonic acid 4 and aniline 5 (10 wt% of 4) in low pH 1.5 aqueous HCl medium using 1.25x equivalent of ammonium persulfate as an oxidizing agent [24], Fig. 2. The elemental compositions of polymer 6 were: C, 28.73; H, 2.70; N, 9.09; S, 22.83; S/2 N ratio 1.25 [Calc. for $C_{36}H_{41}N_{11}S_{10}O_{35}$: (1492); C, 28.97; H, 2.77; N, 10.32; S, 21.48; S/2 N ratio 1.04]. According to the elemental results, the S/2 N ratio is (1:1.25); in other words, every 0.75 aniline unit corresponds to one disulfonated aniline unit, in accordance with their reported analogues [18, 19, 25]. The calculated stoichiometry is close to the theoretical stoichiometry for a repeat unit of copolymer 6. The atomic composition of nitrogen is different than the theoretical value. This discrepancy might be related to the presence of ammonium hydrogen sulfate and/or ammonium chloride that were not able to fully wash out from the precipitated polymer during the working-up step. Targeted Ag@SiO_2 nanocomposite 7 was chemically prepared at rt. by stirring a mixture of Ag@SiO_2 nanoparticles 3, aniline-2,5-disulfonic acid 4, aniline 5 (10 wt% of 4) and L-ascorbic acid (10 wt% of 4) in a 10% HCl/H_2O solution using 1.25x equivalent of ammonium persulfate, Fig. 2, eq. (III). Incorporation of L-ascorbic acid played a dual purpose: as an oxidant and a reactant. The hydrolysis of persulfate is initiated by the homolytic dissociation into the radical anion [$(NH_4)_2S_2O_8 \leftrightarrow 2NH_4^+ + S_2O_8^{2-} \leftrightarrow 2SO_4^{\cdot -}$)], which subsequently propagates the radical chain reaction with sulfonated aniline as shown in Fig. 2. In the meantime, persulfate oxidation of ascorbic acid initiated by the in situ formed radical anion and subsequently, the resulting ascorbo- radical reduced another persulfate molecule

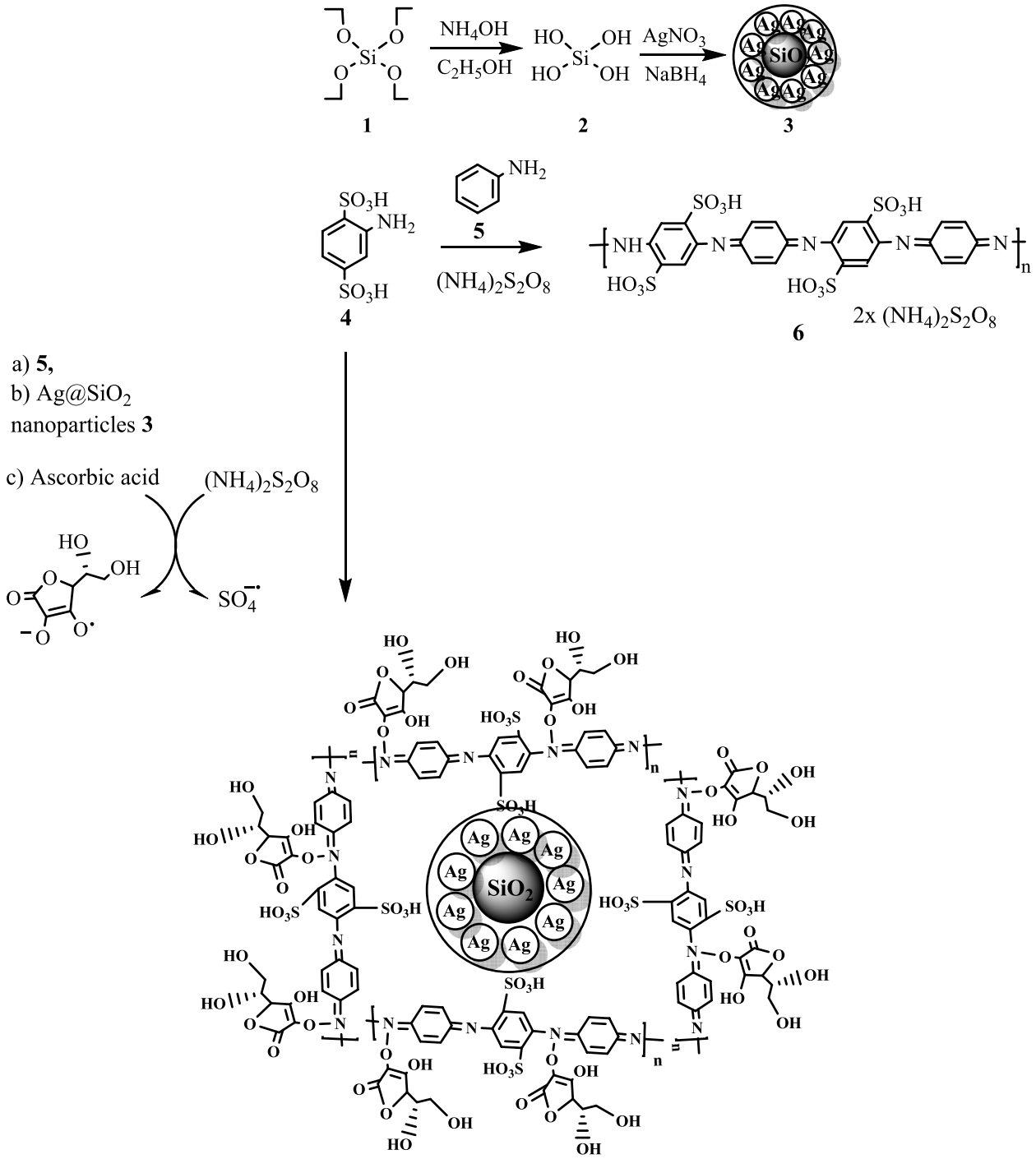

Fig. 2 Chemical synthesis of poly (aniline-co-aniline-2,5-disulfonic acid)/L-hexuronic acid/Ag@SiO_2 nanocomposite 7

to generate a new radical anion, propagating the chain reaction [26]. The elemental compositions of poly (aniline-co-aniline-2,5-disulfonic acid)/L-ascorbic acid/Ag@SiO_2 nanocomposite **7** were C, 46.03; H, 4.58; N, 7.99; S, 5.33; S/2 N ratio 0.33 [Calc. for $C_{42}H_{46}N_6S_2O_{26}$: (1115); C, 45.24; H, 4.16; N, 7.54; S, 5.75 S/2 N ratio 0.38]. According to the experimental elemental results the S/2 N ratio is (1:0.33); in other words, every three aniline units

corresponds to one disulfonated aniline unit, in accordance with their reported analogues [18, 19, 25]. The 0.33 S/2 N ratio found (Calc. 0.38) agrees with the theoretically predicted values. Interestingly, elemental analysis data confirmed the regular presence of the L-ascorbic in the oligomer indicating the electrolytic-rich functionality of the product.

Structure characterization and property measurements

Infrared spectra

The FT-IR spectrum of copolymer 6, Additional file 4: Supplementary 2, exhibited a broad band at approximately υ 3421 cm^{-1} assigned to unresolved NH stretching modes. The N-H bending of aromatic secondary amines also gives an absorption band in the υ 1567 cm^{-1} region. The aromatic C-H peak is seen at υ 1610 cm^{-1}. The peaks at υ 1184 cm^{-1} υ 1042 cm^{-1} correspond to C-H in-plane and out-plane deformations, respectively [18, 19]. The stretching of the benzenoid and quinoid structures is observed at υ 1610 and υ 1582 cm^{-1}, respectively. The aromatic C-N stretching absorption bands appeared at υ 1303 and υ 1239 cm^{-1}. The bands observed at υ 1385 and υ 819 cm^{-1} are due to the C=N stretching of secondary aromatic amines. Absorption between υ 880 and υ 802 cm^{-1} corresponds to C=C bending in 1,2,4,5-tetrasubstituted aromatic structures. Strong asymmetric and symmetric O=S=O stretching vibrations of SO_3^- groups appeared at υ 1144 and υ 1017 cm^{-1}, respectively. The S-O stretching band appeared at υ 726 cm^{-1}, and the peak at υ 663 cm^{-1} corresponds to the C-S stretching vibrational mode. The weak characteristic peaks corresponding to ascorbic acid appeared at υ 3469 cm^{-1} (−OH), υ 1700 (C=O), υ 1639 (C–O stretching), υ 1382, υ 1378 (C–O–C stretching), and υ 670, υ 597 (−OH out of plane deformation). Some additional weak absorption bands appearing at υ 632, υ 622, υ 563, υ 538, and υ 506 cm^{-1} were not assigned. SiO_2@Ag nanocomposite 3, Additional file 4: Supplementary 2, exhibited two characteristic bands at υ 1081 and υ 798 cm^{-1} attributed to stretching of Si–O–Si and Si–O (silanol), respectively. The absorption bands at υ 1459 and υ 1635 cm^{-1} indicate the formation of Ag nanoparticles. The observed small broad band located at υ 3458–3437 cm^{-1} is attributed to the stretching vibration of the O–H bonds confirming the presence of Si–OH and/or adsorbed water. The bands at υ 1500 cm^{-1} and υ 1402–1281 cm^{-1} are attributed to NO_3^- ions and those at υ 465 cm^{-1} are due to Si–O rocking vibrations. The copolymer/L-hexuronic acid/SiO_2@Ag nanocomposite 7, Additional file 4: Supplementary 2, exhibited two characteristic bands at υ 1145 and υ 802 cm^{-1} which are attributed to stretching of Si–O–Si in SiO_4 and Si–O (silanol), respectively. The peak at υ 563 cm^{-1} is due to the bending vibrational mode of the Si–O–Si bond. The absorption bands at υ 1493 indicate the formation of Ag nanoparticles. The observed small band located at υ 3400 cm^{-1} is attributed to the stretching vibration of the Si–OH bond. The small band at υ 454 cm^{-1} is due to Si–O rocking vibrations. Copolymer 6 in the composite exhibited a broad band at approximately υ 3468 cm^{-1}, which was assigned to NH stretching. The N-H bending of aromatic amines gives an absorption band in the υ 1586 cm^{-1} region. The aromatic C-H bond is seen at υ 1609 cm^{-1}. The peaks at υ 1018 cm^{-1} and υ 1405 cm^{-1} correspond to C-H in-plane and out-plane deformations, respectively [16]. The stretching of the benzenoid and quinoid structures is observed at υ 1609 and υ 1570 cm^{-1}, respectively. The absorption bands at υ 1303 and υ 1235 cm^{-1} are characteristic of aromatic C-N stretching. Absorption between υ 881 and υ 819 cm^{-1} was attributed to C=C in 1,2,4,5-tetrasubstituted aromatic structures. The O=S=O vibrations of SO_3^- groups appeared at υ 1144 and υ 1017 cm^{-1}. The S-O band is seen at υ 667 cm^{-1}, and the peak at υ 632 cm^{-1} corresponds to the C-S stretching vibrational mode. The weak characteristic peaks corresponding to ascorbic acid appeared at υ 3480 (−OH), υ 1640 (C–O stretching), υ 1385, υ 1235 (C–O–C stretching), υ 707 and υ 597. Some additional weak absorption bands appearing at υ 538, υ 550, υ 540 and υ 506 cm^{-1} were not assigned. Through comparisons, the FT-IR spectrum of copolymer composite 7 was quite similar to that of copolymer 6, which confirmed the formation of a polymer in the composite. Raw IR data are attached as Additional file 1.

UV absorption

The bandgap energy is calculated from the equation $\Delta E = hc/\lambda$, where ΔE is the bandgap energy (eV), $h = 6.625 \times 10^{-34}$ JS, $c = 3 \times 10^8$ m/s, and λ is the wavelength. The UV—Vis spectrum of the SiO_2@Ag nanocomposite, Additional file 4: Supplementary 3, exhibited the presence of a surface plasmon band in the visible region at λ 420 nm, and its bandgap energy was 2.88 eV which provided evidence for silver composite nanoparticle formation [27]. The electronic spectrum of copolymer 6, Additional file 4: Supplementary 3, shows absorption bands at λ 355 nm, and λ 640 nm, and their bandgap energies were 3.49 eV, and 1.94 eV, respectively. The former peak at λ355 nm is due to the π–π* transition of the benzenoid ring in the extent of conjugation of the adjacent phenyl rings in the chain. Absorption at λ 640 nm is attributed to the quinoid ring transition, and charge transfer from the HOMO of the benzenoid ring to the LUMO of the quinoid ring. This specific absorption is dependent on the overall oxidation state of the polymer [28]. The electronic spectrum of copolymer/SiO_2@Ag nanocomposite 7, Additional file 4: Supplementary 3, shows absorption bands at λ 245 nm, λ 375 nm, and λ 640 nm, and their bandgap

energies were 5.06 eV, 3.31 eV, and 1.94 eV, respectively. The peak at 245 nm is due to the π–π* transition of the benzenoid ring in the extent of conjugation of the adjacent phenyl rings in the chain. The absorption peak near 400 nm confirmed the presence of silver nanoparticles. Absorption at λ 640 nm is attributed to the quinoid ring transition, and charge transfer from the HOMO of the benzenoid ring to the LUMO of the quinoid ring.

Energy-dispersive X-ray spectroscopy (EDXS) analyses

EDXS is a microanalysis of a chemical composition of elements. It is associated with SEM imagery of a specified area to characterize surface morphology. Qualitative analysis involves the identification of the lines in the spectrum, and it is straightforward. Quantitative analysis (determination of the concentrations of the elements present) entails measuring line intensities for each element in the sample and for the same elements in calibration standards of known composition. The chemical composition (wt%) of the sample according to the EDXS spectra of SiO_2@Ag 3, Additional file 4: Supplementary 4; was O, 35.57; Si, 15.87; Ag, 45.28; Cl, 0.16; Na, 0, and that of composite **7**, Additional file 4: Supplementary 4; was C, 35.86; N, 8.22; S, 5.58; O, 35.19; Si, 9.82; Ag, 3.76; Cl, 1.57. Through comparison, it can be concluded that both elemental and EDXS analyses confirmed the successful synthesis of copolymer/SiO_2@Ag nanocomposite 7. Interestingly, both analyses were identical confirming the participation degree of the disulfonated aniline moiety in copolymer backbone 7 by the S/2 N ratio which is equal to 0.33.

Electron microscopy studies

Scanning electron microscopy (SEM) and transmission electron microscopy (TEM) were used as suitable tools to compare and investigate the morphologies of SiO_2/Ag composite 3, copolymer 6, and copolymer/L-hexuronic acid/SiO_2@Ag nanocomposite 7. As shown in Fig. 3, the surface morphology of copolymer 6 was marked by the presence of hemispherical well-separated particles, with an average particle size of 21.5 nm, rather than spherical particles. In the dense area of the image, the sample shows large different sizes and distributions of aggregated spherical morphology. SEM images of SiO_2@Ag composite 3 are shown in Fig. 3. The particles are ordered spherical in shape and well separated from each other, and the average particle size is 19 nm. Silver particles can be clearly seen embedded in the SiO_2 matrix in the samples with higher Ag concentrations, Fig. 3, as supported by the EDXS results given above. SEM images of copolymer/L-hexuronic acid/SiO_2@Ag composite 7 are shown in Fig. 3. The composite displayed intensified spherical particles that were dispersed over almost the entire surface. Specifically, the microstructure of the sample was found to display particles having a spherical shape with a relatively uniform size, 30 nm, on the surface of the SiO_2/Ag matrix. These surface characteristics indicate that the SiO_2/Ag particles penetrated the copolymer hemispherical phase, thereby promoting the formation of the targeted composite as the dominant phase. The particle shapes, compared to copolymer 6, appear almost spherical with a relatively larger average size of 30 nm. In the dense area of the image, the sample shows aggregation of large different sizes and distributions of spherical morphology. Figure 4 shows TEM images of SiO_2/Ag composite 3, copolymer 6, and copolymer/L-hexuronic acid/SiO_2@Ag nanocomposite 7. The size of SiO_2/Ag composite 6 was in the range of 12–13 nm, while that of copolymer 6 was 21.7 nm. As shown in Fig. 3(c), the silver nanoparticles are not fixed on the composite surfaces and, correspondingly, the number of SiO_2 particles in solution is increased; thus, the particle size further increases to form aggregations of increased particle size. As supported by the EDXS results, a fraction of silver particles breaks away from the composite surfaces [29]. Raw SEM images are attached as Additional file 2.

XRD analyses

The XRD spectra in the 2θ range of 5–80° of Ag@SiO_2 nanocomposite 3, copolymer 6 and copolymer/L-ascorbic/SiO_2@Ag nanocomposite 7 are shown in Additional file 4: Supplementary 5. The spectrum of 3 exhibited the characteristic peaks of amorphous silica and crystalline silver at 2θ values of 23.5°, 38.5°, 44.8°, 64.3°, and 77.2° [30], their calculated interatomic spacing values (d) were 0.38 nm, 0.23 nm, 0.20 nm, 0.15 nm, and 0.12 nm, while their crystallite (grain) sizes were 16.96 nm, 17.58 nm, 17.97 nm, 19.61 nm, and 21.25 nm, respectively. The former values are calculated using Bragg's law [31]: order of reflection (n) x wavelength (l) = 2 x interplanar spacing (d) x sin θ, where (n) = 1 and default laser is set at l = 0.15418. The crystallite size values are calculated using the Scherrer eq. [32] Dp = (0.94 x l)/ (b x cos θ); where Dp = average crystallite size, b = line broadening irradiation, θ = Bragg angle, and l = X-ray wavelength. The most intense peak of Ag shows that the crystallinity of Ag increases with increasing Ag concentration. It is suggested that the presence of Ag particles favors crystallization on the formed amorphous silica during the reaction, however, there is no reaction between them to form a new phase. The XRD spectrum of 6 exhibited the characteristic peaks at 2θ values 8.58°, 9.94°, 17.65°, 20.20°, 22.78°, 26.36°, 27.48°, 30.73°, 32.01°, 33.52°, 36.38°, 38.96°, 43.39°, 45.03°, 50.28°, 54.55°, 57.13°, their calculated

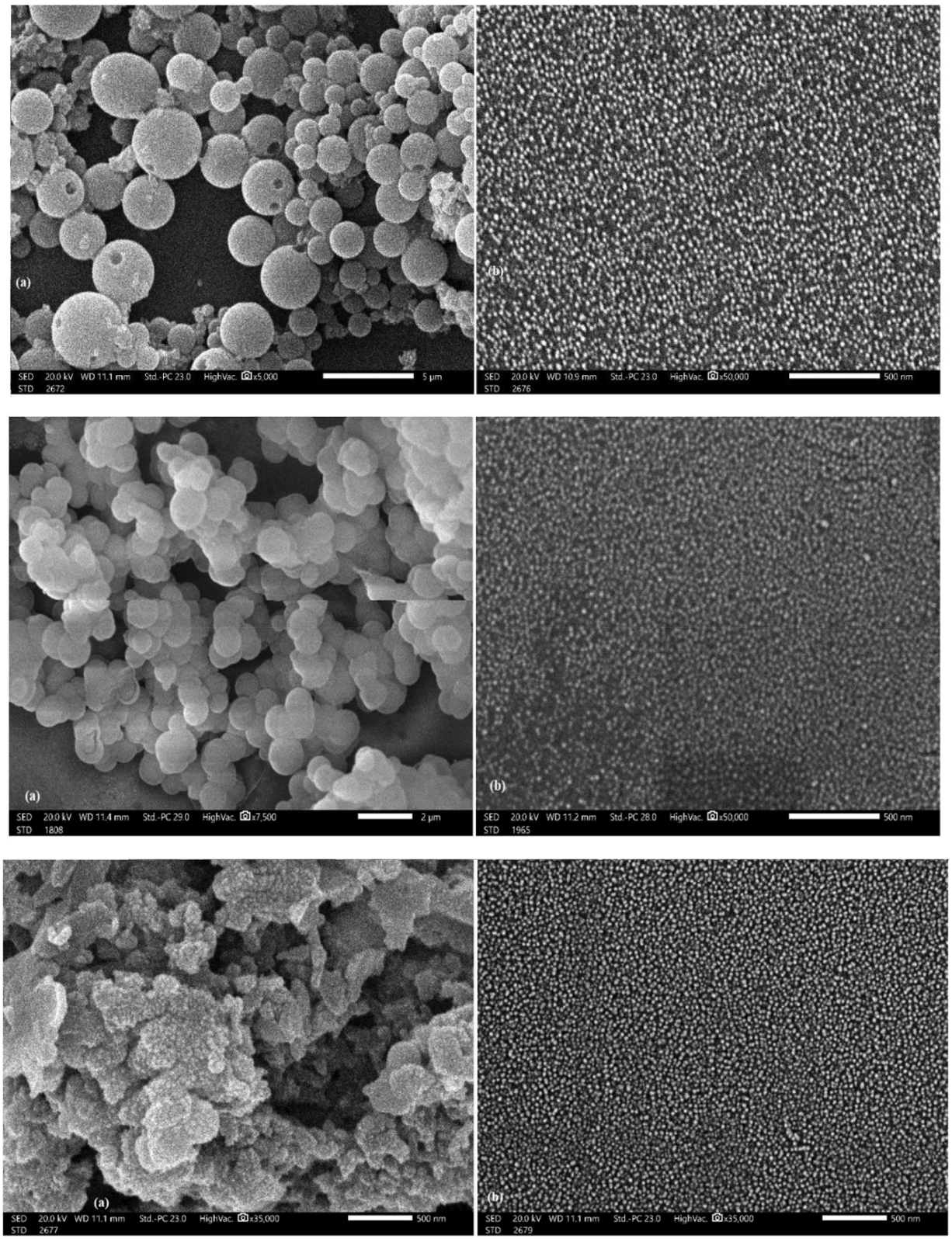

Fig. 3 SEM images of: (upper) Copolymer 6 [scale bar (**a**) 5 µm; **b**) 500 nm]; (middle) The composite SiO_2@Ag **3** [scale bar (**a**) 2 µm; **b**) 500 nm]; and (bottom) the copolymer/L-ascorbic/SiO_2@Ag composite **7**: (**a**) solid state; (**b**) suspension in dioxane

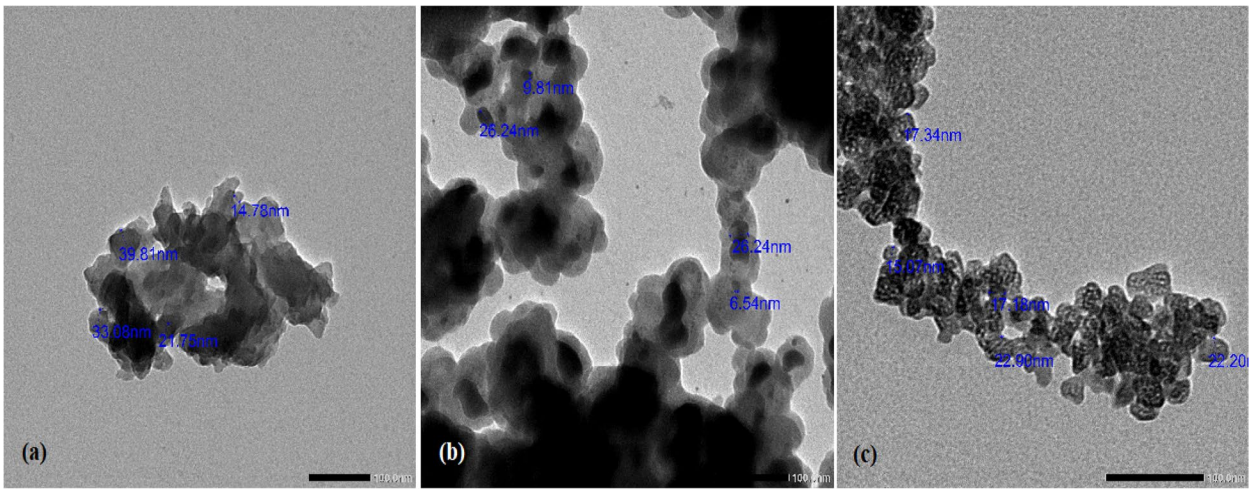

Fig. 4 TEM images of: **a** copolymer 6; **b** SiO_2/Ag composite 3; and **c** copolymer/L-hexuronic acid/SiO_2@Ag nanocomposite 7

interatomic spacing values (d) are 1.03 nm, 0.89 nm, 0.50 nm, 0.44 nm, 0.39 nm, 0.34 nm, 0.32 nm, 0.29 nm, 0.28 nm, 0.27 nm, 0.25 nm, 0.23 nm, 0.21 nm, 0.20 nm, 0.18 nm, 0.17 nm, 0.16 nm, while their crystallite (grain) size are 16.65 nm, 16.66 nm, 16.80 nm, 16.86 nm, 16.93 nm, 17.05 nm, 17.09 nm, 17.22 nm, 17.27 nm, 17.34 nm, 17.47 nm, 17.61 nm, 17.87 nm, 17.97 nm, 18.34 nm, 18.68 nm, and 18.90 nm, respectively. The XRD spectrum of **7** in the 2θ range exhibited the characteristic peaks at 2θ values 9.46°, 18.93°, 20.60°, 24.84°, 27.67°, 32.64°, 33.65°, 37.48°, 44.21°, 46.09°, 54.56°, 57.38°, 64.27°, 67.36°, 74.37°, and 76.58°, their calculated interatomic spacing values (d) are 0.93 nm, 0.47 nm, 0.43 nm, 0.36, 0.32 nm, 0.27 nm, 0.24 nm, 0.20 nm, 0.20 nm, 0.17 nm, 0.16 nm, 0.14 nm, 0.14 nm, 0.13 nm, 0.12 nm, while their crystallite (grain) size are 16.66 nm, 16.83 nm, 16.87 nm, 17.00 nm, 17.10 nm, 17.30 nm, 17.34 nm, 17.53 nm, 17.92 nm, 18.04 nm, 18.68 nm, 19.61 nm, 19.94 nm, 20.84 nm and 21.16 nm, respectively. As reported, the characteristic 2θ value corresponds to van der Waals distances between stacks of phenylene rings to adjacent chains is equal to 25.5° [33, 34]. However, the copolymer 6 and its metallic composite **7** exhibited 2θ values at 26.36° and 27.67°, respectively. This change may be induced by increased separation of the polymer chains due to the presence of side groups and hence, lower the crystallographic order. The side chain -SO_3^- group is likely to force the chain out of planarity by twisting the phenyl rings relative to one another [35]. Generally, the crystallinity and orientation of polymeric chains have been of much interest, because more highly ordered systems strongly influence the composite performance [36]. Raw XRD data are attached as Additional file 3.

Thermal analysis

TG-DTG and DSC curves for poly (aniline-co-aniline-2,5-disulfonic acid) 6 and copolymer/L-hexuronic acid/Ag@SiO_2 nanocomposite 7 are shown in Additional file 4: Supplementary 6 and 7, respectively. The TG thermal degradation curve of copolymer 6 exhibited an interesting model of the stability of the polymer, and its subsequent weight losses could be divided into four steps. The first minor peak from rt. to 225 °C (weight loss 0.59%) could be attributed to the loss of absorbed water. The second minor weight loss at 418 °C (weight loss 23.34%); the strong differential thermogravimetric endothermic peak at 403 °C is likely due to decomposition and/or elimination processes of the side-chain substituents. The third oxidative thermal decomposition of the polymer backbones was suggested to occur above 770 °C (weight loss 25.97%). The remaining polymeric residues (50.09%) were used as the final weight residue. In the DSC curve, the polymer shows an endothermic peak with an energy of 105.15 J/g at 74.6 °C, an endothermic peak of energy 9.23 J/g at 273.4 °C, an endotherm peak of energy 30.87 J/g at 360 °C, two endotherm peaks of energy 81.83 J/g at 404 °C and 34.19 J/g at 482 °C, corresponds to decomposition or elimination processes of the side-chain substituents and the subsequent morphological change in the polymer [37]. DSC of the ligand 6 exhibited gradual endothermic change over a wide range of temperature from room temperature to 780 °C. The first endothermic peak was observed in the range 42 °C – 70 °C resulted from the vaporization of adsorbed

moisture and volatile molecules in polymer matrix. The two exothermic peaks at 74.6 °C and 110 °C correspond to glass transition and material crystallization, respectively, indicating partially crystalline material, and this result was further confirmed by the above-mentioned crystallization peaks in x-ray diffraction. In addition, the sample exhibited successive endothermic degradations at 250 °C, 343 °C and 384 °C attributed to loss of substituents and removal of low molecular weight polymer/oligomer from the polymer matrix. The remaining endotherms at 450 °C and 720 °C are due to the complete degradation and decomposition of the polymer backbone. The TG thermal degradation curve of nanocomposite 7 exhibited an interesting model of the stability of the polymer, and its subsequent weight losses could be divided into three steps. The first minor peak from rt. to 180 °C (weight loss --2.65%) could be attributed to the loss of absorbed water. The second minor weight loss at 414 °C (weight loss − 5.16%) and the third strong differential thermogravimetric endothermic peak at 780 °C (weight loss 8.96%) are likely due to decomposition and/or elimination processes of the side-chain substituents. The DTG spectrum exhibited three endotherm peaks at 130 °C, 305 °C, and 472 °C. The remaining polymeric residues (83.22%) were the final weight residue. In the DSC curve, the polymer shows a weak endothermic peak with an energy of 140.91 J/g at 186 °C and a weak broad endothermic peak centered at 380 °C up to 600 °C. DSC of the composite 7 exhibited an endotherm peak at 93.5 °C attributed to the loss of adsorbed moisture and volatile molecules in composite matrix. The sample exhibited two broad, nearly linear, endothermic degradations at 306 °C, 472 °C attributed to loss of the metallic composite ingredients and the removal of low molecular weight polymer/oligomer from the polymer matrix. The remaining broad endotherm centered nearly at 800 °C is due to the complete backbone decomposition. Worthy to note, DSC curve did not exhibit any exothermic effect, while the above mentioned XRD analysis indicated less ordered and less intense crystalline pattern. This could be attributed to the slow crystallization and the evolved heat flow over large temperature range was lost in the baseline scatter. Because the gradual melting peaks of the metallic composite 7 are higher than that of the organic copolymer 6, it is rational to conclude that the presence of $Ag@SiO_2$ contents in the composite 7 increased its thermal stability.

Cyclic voltammetry

It is well known in the literature that polyaniline in both doped and intrinsic states can exist in three different discrete oxidation states at the molecular level depending on the relative number of benzenoid and quinoid units in the polymer. These states are known as the completely reduced leucoemeraldine, emeraldine and fully oxidized pernigraniline states, which all become protonated after doping. Therefore, its redox processes in 1 M HCl have two redox peaks: the first peak (leucoemeraldine ↔ emeraldine) has an $E_{1/2} = 0.18$ V vs Ag/AgCl (saturated) and the second (emeraldine ↔ pernigraniline) an $E_{1/2} = 0.77$ V [35]. The cyclic voltammogram of copolymer 6, Fig. 5(a), exhibited two pairs of redox peaks at − 0.11 µA /0.06 V and 0.14 µA /0.24 V, while the two pairs of redox peaks are in 0.25 µA /0.14 V and 0.04 µA /− 0.14 V. The cyclic voltammogram of copolymer/L-ascorbic/SiO_2@Ag nanocomposite **7**, Fig. 5 (b), exhibited three redox peaks at − 0.14 µA/0.004 V, − 1.47 µA /0.11 V and − 2.85 µA /0.18 V, and the other four redox peaks are at − 1.92 µA /0.22 V, − 0.007 µA /0.160 V, 1.30 µA /0.069 V and 2.81 µA /0.007 V, respectively. The influence of the presence of aniline disulfate copolymerized with aniline is similar to that of the aniline/orthanilic acid copolymer reported by Xu et al. [25]. The redox potential

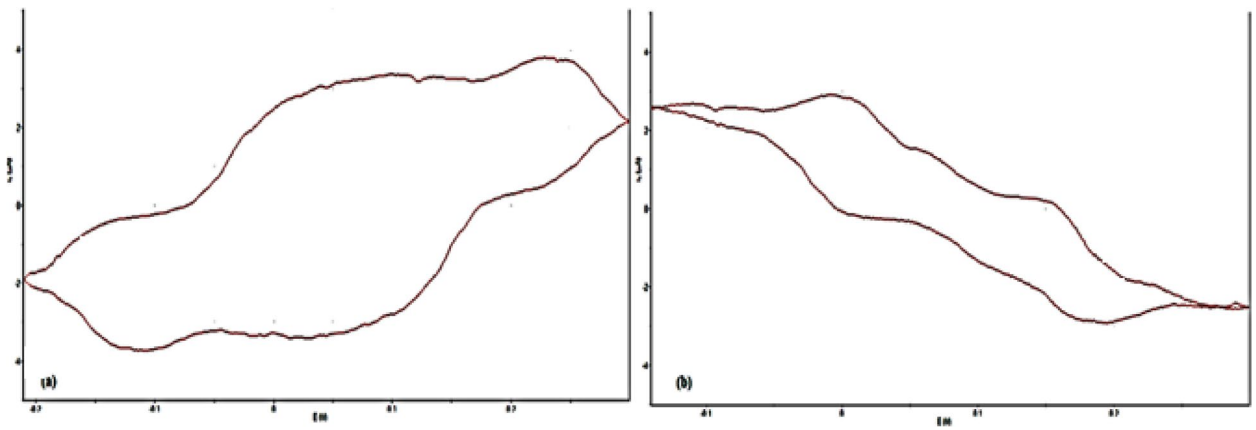

Fig. 5 Cyclic voltammetry (50 mV/s) of: (**a**) copolymer 6; and (**b**) copolymer/L-hexuronic acid/SiO_2@Ag nanocomposite 7 in DMSO solutions

of aniline/orthanilic acid copolymer (1:1), (1:2) and (1:4) was similar to polyaniline, whose first transition potential is 0.18 V and the second one is 0.7 V. However, in the cases of aniline/orthanilic acid copolymer (1:6) and (1:8) in 1.0 mol/L H_2SO_4 media, there were two pairs of redox peaks in the former at 0.29 µA /0.17 V and 0.56 µA /0.45 V, while the latter exhibited two pairs of redox peaks at 0.32 µA/0.23 V and 0.53 µA/0.43 V, respectively. This means that the difference in the (aniline: orthanilic acid) ratios in the copolymer strongly affects the redox potential values of the product. For instance, the higher incorporation of sulfonated aniline units into

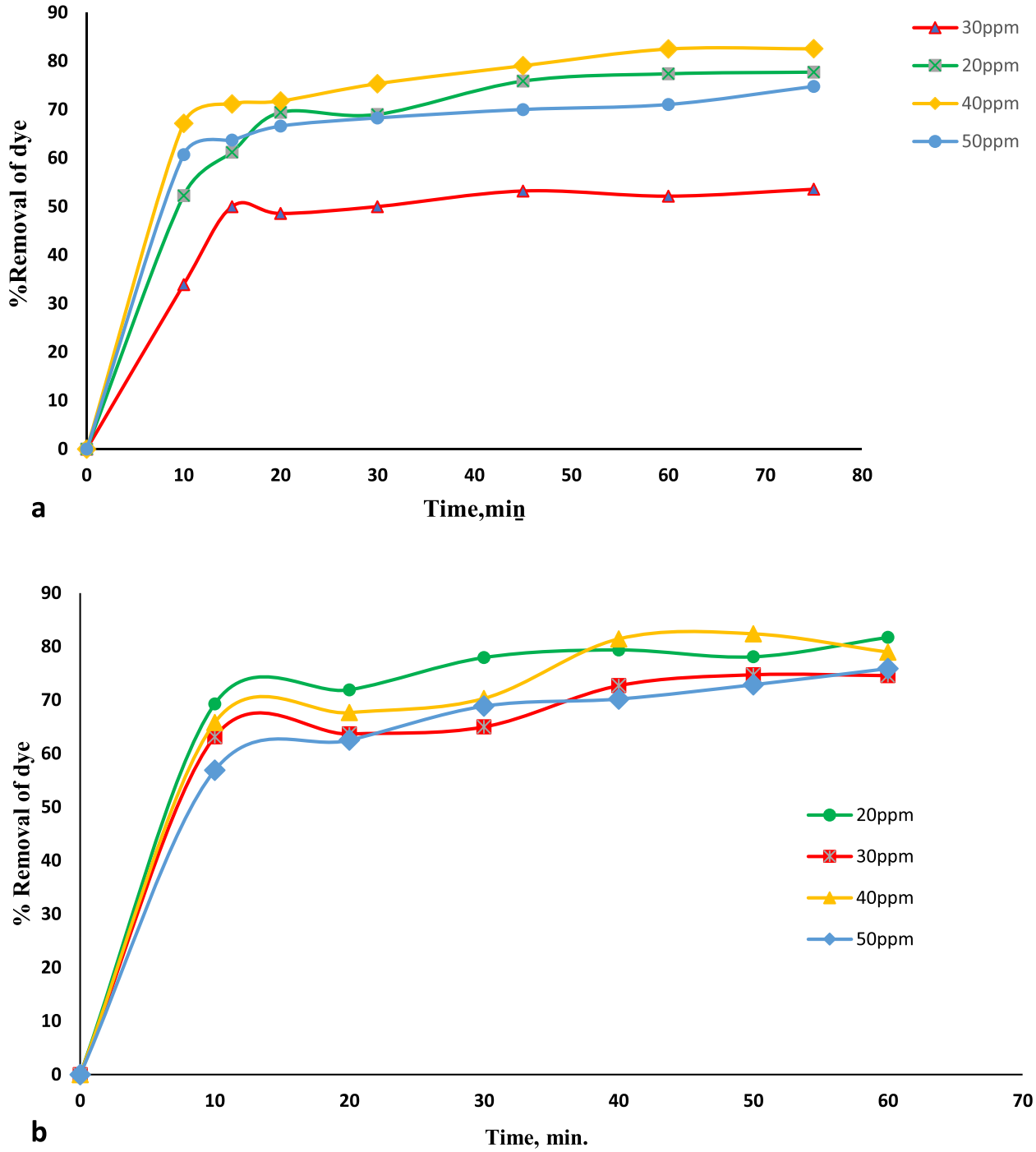

Fig. 6 Effect of contact time on: (**a**) Copolymer **6** (2 g/L), and (**b**) Composite **7** (2 g/L) on % removal of safranine dye at different concentrations, pH = 7.2, 25 °C

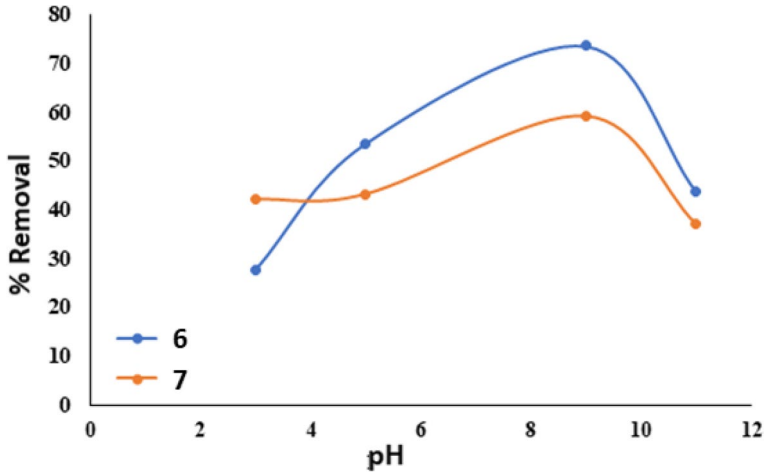

Fig. 7 Effect of pH on the % removal of 30 ppm safranine dye for copolymer 6 and composite 7 (2 g/L) at 25 °C within 45 min

the copolymer leads to a lower potential energy for the second redox process [25]. This result is attributed to the steric hindrance and ineffective delocalization of the positive charge around nitrogen atoms could lead to an increase in the energy barrier to bipolaron formation, i.e., difficulty in the oxidation of the nitrogen atoms which results in a more positive potential energy for the first transition and a more negative potential energy for the second transition. With comparison to the insertion of a unit of orthanilic acid, the insertion of a unit of aniline disulfate results in two sulfonate side-groups in the same benzene ring and the second process in the aniline-aniline disulfate copolymer is more effective than that in the aniline-orthanilic acid copolymer [25].

Adsorption studies of safranine dye

Effect of contact time To establish an equilibrium time for maximum uptake and to determine the kinetics of the adsorption process, the adsorption of safranine dye on 6 and 7 as adsorbents was studied as a function of contact time and the results are shown in Fig. 6. It was found that the rate of uptake of safranine dye using 6 is rapid in the beginning in the range of 34% to 67% for different dye concentrations, Fig. 6 (a), and in the range of 53.5% to 82.5% adsorption is complete within 75 min. The time required to achieve equilibrium is 45 min. For 7, the rate of uptake of safranine dye is faster than using 6, that is in the range of 56.8% to 69.2% in the beginning for different dye concentrations, Fig. 6 (b), and in range of 53.5% to 82.5% adsorption is complete within 75 min. The time required to achieve equilibrium is 45 min in the range of 75.8% to 81.7%, attributed to more vacant sites in adsorbent active surface until reach equilibrium state and higher interaction between the safranin cations and sequestering adsorbent sites. These results are qualitatively in good agreement with those reported in the literature [38].

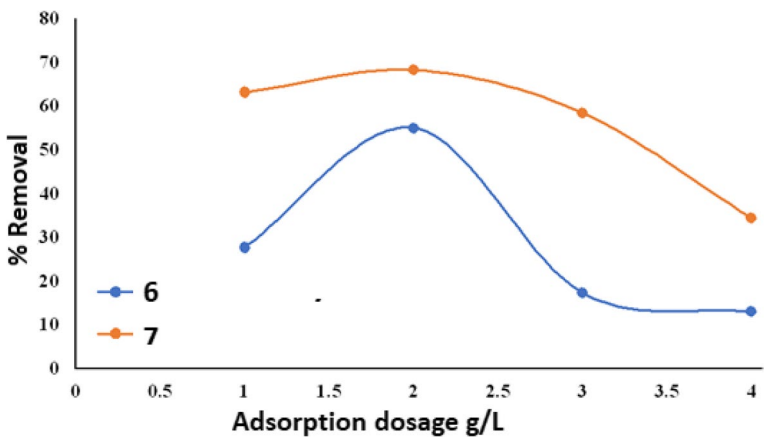

Fig. 8 Effect of adsorption dosage on % removal of 30 ppm safranine dye for copolymer 6 and composite 7 (2 g/L), pH 6.5, at 25 °C within 45 min

Effect of pH The influence of pH on the adsorption properties of safranin using 6 and 7 was studied as one of the main factors that control the adsorption mechanisms of the studied solid adsorbents. The initial pH of the operating systems affects the speciation of the present pollutant ions in the solutions as well as the surface properties of the solid adsorbent as it can promote the protonation or deprotonation of the dominant surficial chemical functional groups [39]. The adsorption of safranin dye on 6 and 7 was monitored over a range of pH values from 3 to 11 of individual solutions, Fig. 7. Low percent removal was observed at pH 3. The removal efficiency of safranin reached maximum values of 73.6% for 6 and 59.3% for 7 at pH 9. The safranin's amino groups ($-NH_2$) are protonated at low pH values by acidic aqueous medium, while the sulfonic acid groups on the adsorbent under such conditions are intact in the dye solution. Therefore, a low electrostatic attraction exists and hence, acidic low pH values do not favor the adsorption of the cationic dye. As the pH of the system increases, free unpaired electrons become available on the terminal dye's amino groups, which in turn will increase the electrostatic attraction forces with the adsorbent sulfonate sites resulting in a high adsorption capacity at higher pH values [40].

Effect of adsorbent dosage The adsorbent dosage is an essential parameter because it determines the maximum capacity of an adsorbent for a given dye concentration. The % removal for safranin dye as a function of adsorbent dosage using 6 and 7 was investigated, Fig. 8. The maximum percentages of dye removal were 55% and 68.3%, respectively, and then decreased with the adsorbent dose up to 4 g/L. The reduction in the removal percentage of safranin dye could be attributed to overcrowding of adsorbent molecules that may prohibit accurate dye/adsorbent particle binding [41].

Adsorption isotherm study

The isotherm of dye adsorption interprets the interaction with the adsorbent and highlights its importance to optimize the application of adsorbents. Therefore, the adsorption isotherms can explain the relationship between the dye removal capacity and the initial dye concentration at constant temperature and equilibrium.

Langmuir isotherm The Langmuir isotherm model [42] specifies monolayer adsorption of safranin dye onto 6 and 7 without interaction between adsorbed ions. The linear form of the Langmuir isotherm equation is represented by eq. (3):

$$\frac{C_e}{q_e} = \frac{1}{Q^0 b} + \frac{1}{Q^0} C_e \tag{3}$$

where Q^0 is the maximum metal ion uptake per unit mass of adsorbent (mg/g) related to adsorption capacity, b is the Langmuir constant (L/mol) related to the energy of sorption, C_e: is the equilibrium concentration, mg/l and q_e: is the equilibrium adsorption capacity, mg/g. Therefore, a plot of Ce/qe versus Ce, gives a straight line of slope $1/Q^0$ and intercept $1/(Q^0 b)$. The results obtained from the Langmuir model for the removal safranine dye shown in table (1) indicate that the safranin dye is mostly adsorbed as a monolayer onto the adsorbents and the results reflected very high fitness which was reflected clearly in the values of the determination coefficients (R^2 more than 0.9) for polymers 6 and 7. Thus, the maximum adsorbed quantities for the dissolved contaminants can be achieved after saturation of all the present adsorption receptor sites by the captured pollutants from water [43]. Hence, the Langmuir isotherm is the optimum model to represent the uptake of safranin dye by copolymer 6 and composite 7.

Table 1 Langmuir and Freundlich models for the removal safranin dye by copolymer 6 and composite 7

Isotherm model	6	7
Langmuir model		
Q0 (mg g^{-1})	71.43	82.64
b (L mg^{-1})	0.027	0.027
R2	0.93	0.91
Freundlich model		
1/n	0.712	0.697
kf	2.822	3.348
R2	0.852	0.815

Table 2 Different kinetic model parameters for the removal of safranin dye by copolymer 6 and composite 7

Isotherm model	6	7
Pseudo first-order kinetics model (safranine dye50ppm)		
k_1 (min^{-1})	0.1088	0.0699
q_e exp. (mg/g)	17.5	18.2
q_e cal (mg/g)	17.7	18.6
R^2	0.91	0.957
Pseudo second-order kinetics model (safranine dye50ppm)		
k_2 (g/mg. min)	0.0259	0.0192
q_e exp. (mg/g)	17.5	18.2
q_e cal (mg/g)	17.7	18.6
R^2	0.9975	0.994

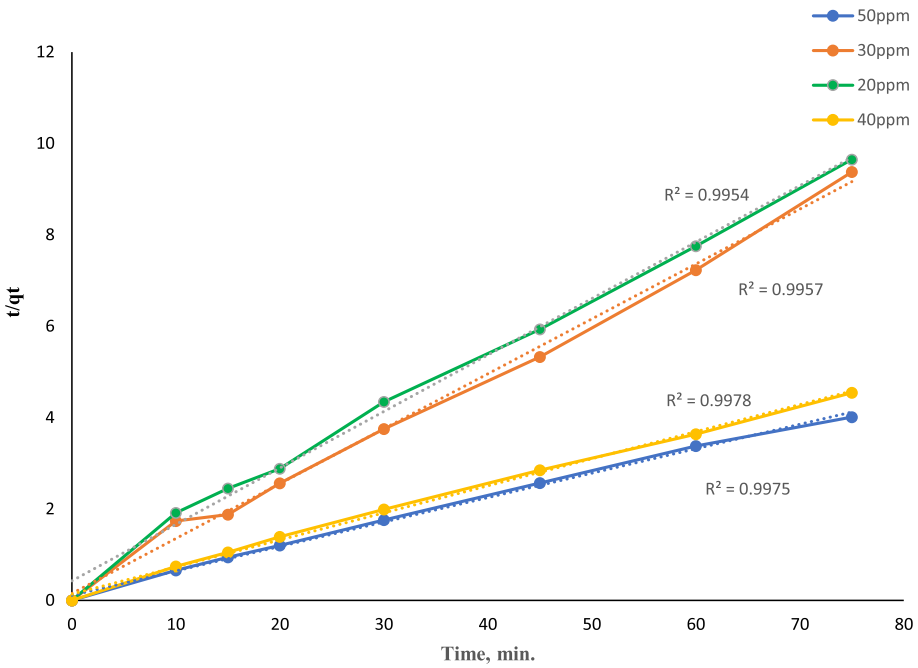

Fig. 9 Pseudosecond-order plot for oligomer 6

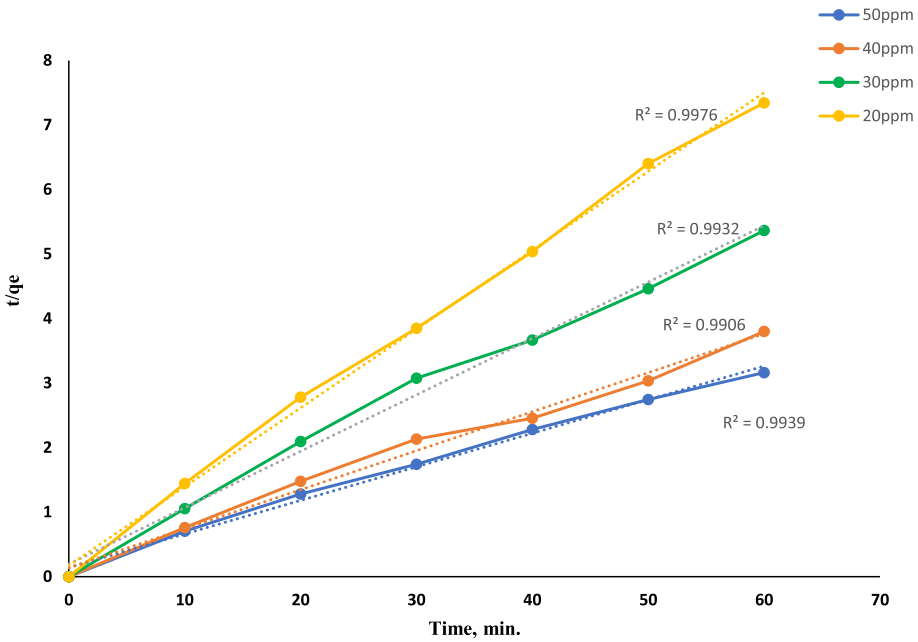

Fig. 10 Pseudosecond-order plot for composite 7

The Freundlich isotherm The Freundlich isotherm [42] describes the adsorption equation for nonideal adsorption that involves heterogeneous adsorption and multilayer coverage of safranin dye onto 3 and 7 surfaces. This empirical isotherm is expressed by eq. (4):

$$q_e = K_F C_e^{\frac{1}{n}} \tag{4}$$

The equation is conveniently used in the linear form by taking the logarithm of both sides as:

$$\log q_e = \log K_F + \frac{1}{n} \log C_e \quad (5)$$

The Freundlich constants, K_F and 1/n, are related to the adsorption capacity and intensity of adsorption, respectively. The values of n and K_F can be calculated from the slope and intercept of the plot of log q_e versus log C_e derived from Eq. (5). The magnitude of the exponent 1/n gives an indication of the favorability of adsorption; for a perfect heterogeneous surface, the value of 1/n should be close to zero. Theoretical calculations indicated that $R^2 = 0.852$ and 0.815 for 6 and 7, respectively, Table 1.

Kinetic studies

Different kinetic models are used to analyze the experimental data. The pseudofirst-order model is conceptualized on the capacity of adsorbents for dye uptake, Eq. (6). It also assumes that the absorption on the sorption sites depends on the empty, i.e., unoccupied adsorbent sites, and these are directly proportional [44]. The rate constant (k_1) is estimated by plotting ln (q_e-q_t) against time [45]. The pseudosecond-order model presumes that dye is removed through chemisorption and physisorption [46]. Data fitting in this model determines the rate-controlling step's feasibility [47]. The rate constant(k_2) is estimated by plotting t/qt against t, as shown in Eq. (7). High R^2 values (more than 0.99) and little difference between expected and calculated q_e specify that kinetic data, Table 2, are best fitted in pseudosecond-order model for safranin dye removal using 6, Fig. 9, and 7, Fig. 10.

$$\ln (q_e + q_t) = \ln q_e - k_1 t \quad (6)$$

$$\frac{t}{q_t} = \frac{1}{q_e^2 k_2} + \frac{t}{q_e} \quad (7)$$

where q_t and q_e are the amounts of the adsorbate adsorbed at any time and equilibrium (mg/g), respectively, k_1 is the pseudo 1st order adsorption rate constant, and k_2 is the pseudo 2nd order adsorption rate constant.

Comparison with literature

A comparison of safranin adsorption efficiency of the synthesized material with other reported material in the same domain suggested that the present composite was more efficient because it was able to remove 19 mg of the dye using 0.02 g within 75 min, while the photocatalytic removal of only 5 mg / L of the dye using polypyrrole nanofiber/Zn-Fe layered double hydroxide was achieved after 120 min illumination time using 0.05 g of the composite [4].

Conclusion

We report the chemical synthesis of sulfonated polyaniline/L-hexuronic acid/Ag/SiO_2 nanocomposite as a new highly anionic polyelectrolyte with an enhanced adsorptive effect for removing the cationic dye safranin. The composite structure was characterized with various analytical techniques like IR, UV, cyclic voltammetry, SEM, TEM, TGA, and DSC. Interestingly, elemental and EDXS results were identical to unambiguously confirm the participation degree of the disulfonated aniline moiety in the copolymer backbone. SEM and TEM images of the SiO_2@Ag nanospheres exhibited well-separated spherical particles with an average size of 10 nm. The surface morphology of the organic copolymer was marked by the presence of hemispherical well-separated particles with an average size of 21.5 nm. SEM and TEM images of the targeted nanocomposite displayed intensified spherical particles that were dispersed over almost the entire surface, and the SiO_2/Ag particles were distributed on the composite surface. The XRD spectrum exhibited peaks of amorphous silica and crystalline silver at many 2θ values, and their interatomic spacing values (d) and crystallite (grain) sizes were calculated. The 2θ values indicated that the side chain sulfonic group is likely to force the polymeric chain out of planarity by twisting the phenyl rings relative to one another and lower crystallographic order. The thermal degradation curve of the organic copolymer or the composite exhibited an interesting model of the stability of the polymer, and their subsequent weight losses were completed in four steps, leaving more than 50% of their weights as a remaining residue. The detected glass transition and crystallization peaks in DSC curves further confirmed the composite partial crystalline nature and the presence of Ag@SiO_2 contents increased its thermal stability. The cyclic voltametric results indicated that the prepared organic copolymer or its Ag@SiO_2 nanocomposite exhibited redox peaks like that reported of its analogue derived from aniline/orthanilic acid copolymer.

To evaluate the efficiency of copolymer and its Ag@SiO_2 composite as adsorbents for safranin-dye in aqueous medium, the effects of experimental parameters such as pH, adsorbent dose, contact time, and dye concentration were studied, and results are summarized as follows:

- The dye uptake rate using nanocomposite was rapid than using the organic copolymer and the maximum dye removal achieved was 82.5% within 75 min.
- The safranin removal efficiency reached maximum values of 73.6% and 59.3% by the two tested absorbents at pH 9.

- The maximum percentage dye removal as a function of adsorbent dosage 2 g/L by the two tested absorbents were 55% and 68.3% and then decreased at higher adsorbent doses.
- The Langmuir isotherm model was optimum to optimize the application of adsorbents and the calculated maximum adsorption capacities of the copolymer and its metallic composite were $71.43\,mg\,g^{-1}$ and $82.64\,mg\,g^{-1}$, respectively, at room temperature.
- The uptake of safranin by the copolymer and its Ag@SiO_2 composite was well defined by pseudo second order model, with rate constant $K_2 = 0.03\,g\,mg^{-1}\,min^{-1}$ for $17.5\,mg\,g^{-1}$ and $0.02\,g\,mg^{-1}\,min^{-1}$ for $18.2\,mg\,g^{-1}$, respectively.

A comparison of safranin adsorption efficiency using the synthesized sulfonated polyaniline copolymer or its Ag@ SiO_2 nanocomposite with other reported material in the same domain suggested that the present crystalline composite has a higher adsorption rate and capacity. The ongoing research is devoted to improving the removal percentage of the dye by using symmetric 1,3,5-triazine based sulfonated polyaniline/Ag@ SiO_2 nanocomposite. The 1,3,5-triazine unit has been used as a key functional group in host-guest chemistry, mainly based on generation of organized aggregates via strong three simultaneous hydrogen bonds formation.

Supplementary Information

The online version contains supplementary material available at https://doi.org/10.1186/s42252-023-00038-y.

Additional file 1.

Additional file 2.

Additional file 3.

Additional file 4.

Authors' contributions

H.H.: Developed and supervised the research, performed the experimental preparation, analysed all characterization data, and wrote all data in the final form. M.A.: Performed the dye adsorption measurements, analysed the data, and wrote the draft of discussion of this section. All authors discussed the results and contributed to the final manuscript. The authors read and approved the final manuscript.

Availability of data and materials

All data generated or analyzed during this study are included in this published article [and its supplementary document].

Declarations

Ethics approval and consent to participate

Not applicable.

Consent for publication

Not applicable.

Competing interests

The authors declare no competing interests.

Received: 10 November 2022 Accepted: 26 January 2023
Published online: 13 February 2023

References

1. D.A. Yaseen, M. Scholz, Textile dye wastewater characteristics and constituents of synthetic effluents: A critical review. Int. J. Environ. Sci. Technol. **16**, 1193–1226 (2019). https://doi.org/10.1007/s13762-018-2130-z
2. M.T. Yagub, T.K. Sen, S. Afroze, H.M. Ang, Dye and its removal from aqueous solution by adsorption: A review. Adv. Colloid Interf. Sci. **209**, 172–184 (2014). https://doi.org/10.1016/j.cis.2014.04.002
3. G. Ciric-Marjanovi'c, N.V. Blinova, M. Trchova, J. Stejskal, Chemical oxidative polymerization of safranines. J. Phys. Chem. B **111**, 2188–2199 (2007). https://doi.org/10.1021/jp067407w
4. F. Mohamed, M.R. Abukhadra, M. Shaban, Removal of safranin dye from water using polypyrrole nanofber/Zn-Fe layered double hydroxide nanocomposite (PPyNF/Zn-Fe LDH) of enhanced adsorption and photocatalytic properties. Sci. Total Environ. **640–1**, 352–363 (2018). https://doi.org/10.1016/j.scitotenv.2018.05.316
5. M.R. Abukhadra, M. Shaban, F. Sayed, I. Saad, Efficient photocatalytic removal of safranin-O dye pollutants from water under sunlight using synthetic bentonite/polyaniline@Ni_2O_3 photocatalyst of enhanced properties. Environ. Sci. Pollut. Res. **25**, 33264–33276 (2018). https://doi.org/10.1007/s11356-018-3270-x
6. M.R. Abukhadra, M. Shaban, M.A. Abd El Samad, Enhanced photocatalytic removal of Safranin-T dye under sunlight within minute time intervals using heulandite/polyaniline@nickel oxide composites a novel photocatalyst. Ecotoxicol. Environ. Saf. **162**, 261–271 (2018). https://doi.org/10.1016/j.ecoenv.2018.06.081
7. D. Karadag, E. Akgul, S. Tok, F. Erturk, M.A. Kaya, M. Turan, Basic and reactive dye removal using natural and modified zeolites. Chem. Eng. Data **52-6**, 2436–2441 (2007). https://doi.org/10.1021/je7003726
8. M. Anjum, R. Miandad, M. Waqas, F. Waqas, M.A. Barakat, Remediation of wastewater using various nanomaterial. Arab. J. Chem. **12**, 4897–4919 (2019). https://doi.org/10.1016/j.arabjc.2016.10.004
9. C. Fleischmann, M. Lievenbrück, H. Ritter, Polymers and dyes: Developments and applications. Polymers **7**, 717–746 (2015). https://doi.org/10.3390/polym7040717
10. E.N. Zarea, A. Motaharib, M. Sillanpää, Nano-adsorbents based on conducting polymer nanocomposites with main focus on polyaniline and its derivatives for removal of heavy metal ions/dyes: A review. Environ. Res. **162**, 173–195 (2018). https://doi.org/10.1016/j.envres.2017.12.025
11. V. Babel, B.L. Hiran, A review on polyaniline composites: Synthesis, characterization, and applications. Polym. Compos. **42**, 3142–3157 (2021). https://doi.org/10.1002/pc.26048
12. S. Agarwal, I. Tyagi, V.K. Gupta, F. Golbaz, A.N. Golikand, O. Moradi, Synthesis and characteristics of polyaniline/zirconium oxide conductive nanocomposite for dye adsorption application. J. Mol. Liq. **218**, 494–498 (2016). https://doi.org/10.1016/j.molliq.2016.02.040
13. M. Rastgordani, J. Zolgharnein, V. Mahdavi, Derivative spectrophotometry and multivariate optimization for simultaneous removal of titan yellow and Bromophenol blue dyes using polyaniline@SiO_2 nanocomposite. Microchem. J. **155**, 104717 (2020). https://doi.org/10.1016/j.microc.2020.104717
14. M.A. Salem, R.G. Elsharkawy, M.F. Hablas, Adsorption of brilliant green dye by polyaniline/silver nanocomposite: Kinetic, equilibrium, and thermodynamic studies. Eur. Polym. J. **75**, 577–590 (2016). https://doi.org/10.1016/j.eurpolymj.2015.12.027
15. M. Abbasian, P. Niroomand, M. Jaymand, Cellulose/polyaniline derivatives nanocomposites: Synthesis and their performance in removal of anionic dyes from simulated industrial effluents. J. Appl. Polym. Sci. **134**, 45352 (2017). https://doi.org/10.1002/app.45352
16. X.L. Wei, Y.Z. Wang, S.M. Long, C. Bobeczko, A.J. Epstein, Synthesis and physical properties of highly Sulfonated Polyaniline. J. Am. Chem. Soc. **118**, 2545–2555 (1996). https://doi.org/10.1021/ja952277i

17. G. Chakraborty, A. Bhattarai, R. De, Polyelectrolyte–dye interactions: An overview. Polymers **14**, 598 (2022). https://doi.org/10.3390/polym14030598
18. D.E. Abd-El-Khalek, H.H.A.M. Hassan, S.R. Ramadan, Water-soluble sulfonated polyaniline as multifunctional scaling inhibitor for crystallization control in industrial applications. Chem. Eng. Res. Des. **169**, 135–141 (2021). https://doi.org/10.1016/j.cherd.2021.03.004
19. Zein El-Din AM, Hassan HHAM, Abou El-Kheir MM,Youssef RM, Controlling soil surface crust formation using Nanosized sulfonated polyaniline. J Soil & Water Con. (Unified Journals) **1**, 001–009 (2016)
20. H.H.A.M. Hassan, D.E. Abd-El-Khalek, M. Abdel Fattah, Synthesis and assessment of poly (5-nitro-2-aminophenol) as a new scaling inhibitor on controlling the precipitation of $CaCO_3$ and $CaSO_4$ in solution. J. Polym. Res. **29**, 255 (2022). https://doi.org/10.1007/s10965-022-03104-4
21. Hassan HHAM, Abd-El-Khalek DE, Abdel Fattah M Assessment of self-doped poly (5-nitro-2-orthanilic acid) as a scaling inhibitor to control the precipitation of CaCO3 and CaSO4 in solution. Sci Reports **12**, 9722. https://doi.org/10.1038/s41598-022-13564-9
22. H. Tang, A. Kitani, T. Yamashita, S. Ito, Highly sulfonated polyaniline electrochemically synthesized by polymerizing aniline-2,5-disulfonic acid and copolymerizing it with aniline. Synth. Met. **96**, 43–48 (1998). https://doi.org/10.1016/S0379-6779(98)00061-7
23. Y.S. Shin, M. Park, H.Y. Kim, F.L. Jin, S.J. Park, Synthesis of silver-doped silica-complex nanoparticles for antibacterial materials. Bull. Korean Chem. Soc. **35**, 2979–2984 (2014). https://doi.org/10.5012/bkcs.2014.35.10.2979
24. J. Stejskal, R.G. Gilbert, Polyaniline: Preparation of conducting polymer (IUPAC technical report). Pure Appl. Chem. **74**, 857–867 (2002). https://doi.org/10.1351/pac200274050857
25. Y. Xu, L. Dai, J. Chen, J.Y. Gal, H. Wu, Synthesis and characterization of aniline and aniline-o-sulfonic acid copolymers. Eur. Polym. J. **43**, 2072–2079 (2007). https://doi.org/10.1016/j.eurpolymj.2006.09.017
26. J. Shen, P.T. Grifths, S.J. Campbell, B. Utinger, M. Kalberer, S.E. Paulson, Ascorbate oxidation by iron, copper and reactive oxygen species: Review, model development, and derivation of key rate constants. Sci. Report. **11**, 7417 (2021). https://doi.org/10.1038/s41598-021-86477-8
27. S.Y. Zhao, S.H. Chen, D.G. Li, X.G. Yang, H.Y. Ma, A convenient phase transfer route for Ag nanoparticles. Physica E Low-dimensional Syst. Nanostruct. **23**(1–2), 92–96 (2004). https://doi.org/10.1016/j.physe.2004.01.008
28. M.F. Zainal, Y. Mohd, Characterization of PEDOT films for electrochromic applications. Polym.-Plast. Technol. Eng. **54**, 276–281 (2015). https://doi.org/10.1080/03602559.2014.977422
29. K. Patil, X. Wang, T. Lin, Electrostatic coating of cashmere guard hair powder to fabrics: Silver ion loading and antibacterial properties. Powder Technol. **245**, 40–47 (2013). https://doi.org/10.1016/j.powtec.2013.04.015
30. S. Sembiring, A. Riyanto, I. Junaidi, R. Situmeang, Structure and properties of silver-silica composite prepare from rice husk silica and silver nitrate. Ceramics-Silikáty **66**(2), 67–177 (2022). https://doi.org/10.13168/cs.2022.0011
31. W.L. Bragg, *The Crystalline State. Vol 1* (The Macmillan Company, New York, 1934) https://archive.org/details/crystallinestate01brag
32. P. Scherrer, Estimation of the size and internal structure of colloidal particles by means of Rontgen rays. Nachr Ges Wiss Göttingen **26**, 98–100 (1918)
33. C. Saravanan, S. Palaniappan, F. Chandezon, Synthesis of nanoporous conducting polyaniline using ternary surfactant. Mater. Lett. **62**, 882–885 (2008)
34. Karthik, R; Meenakshi, S, Removal of hexavalent chromium ions using Polyaniline/silica gel composite. J. Water Process Eng. **1**, 37–45 (2014)
35. J. Yue, Z.H. Wang, K.R. Cromack, A.J. Epstein, A.G. MacDiarmid, Effect of sulfonic acid group on Polyaniline backbone. J. Am. Chem. Soc. **113**, 2665–2671 (1991). https://doi.org/10.1021/ja00007a046
36. H. Xia, Q. Wang, Ultrasonic irradiation: A novel approach to prepare conductive polyaniline/nanocrystalline titanium oxide composites. Chem. Mater. **I**, 2158–2165 (2002)
37. A.N. Andriianova, Y.N. Biglova, A.G. Mustafin, Effect of structural factors on the physicochemical properties of functionalized polyanilines. RSC Adv. **10**, 7468–7491 (2020). https://doi.org/10.1039/C9RA08644G
38. K.M. Elsherif, A. El-Dali, A.M. Ewlad-Ahmed, A. Treban, I. Alttayib, Removal of Safranin dye from aqueous solution by adsorption onto olive leaves powder. J. Mater. Environ. Sci. **12**(3), 418–430 (2021)
39. D. Ozdes, A. Gundogdu, B. Kemer, C. Duran, H.B. Senturk, M. Soylak, Removal of Pb(II) ions from aqueous solution by a waste mud from copper mine industry: Equilibrium, kinetic and thermodynamic study. J. Hazard. Mater. **166**, 1480–1487 (2009). https://doi.org/10.1016/j.jhazmat.2008.12.073
40. J. Azimvand, K. Didehban, S.A. Mirshokraie, Safranin-O removal from aqueous solutions using lignin nanoparticle-g-polyacrylic acid adsorbent: Synthesis, properties, and application. Adsorpt. Sci. Technol. **36**(7–8), 1422–1440 (2018). https://doi.org/10.1177/0263617418777836
41. V.K. Garg, R. Gupta, A.B. Yadav, R. Kumar, Dye removal from aqueous solution by adsorption on treated sawdust. Bioresour. Technol. **89**(2), 121–124 (2003). https://doi.org/10.1016/s0960-8524(03)00058-0
42. I. Langmuir, The adsorption of gases on plane surfaces of glass, mica and Platinum. J. Am. Chem. Soc. **40**, 1361–1368 (1918). https://doi.org/10.1021/ja02242a004
43. S.J. Allen, Q. Gan, R. Matthews, P.A. Johnson, Comparison of optimized isotherm models for basic dye adsorption by kudzu. Bioresour. Technol. **88**(1), 143–152 (2003). https://doi.org/10.1016/s0960-8524(02)00281-x
44. R.K. Gautam, P.K. Gautam, S. Banerjee, V. Rawat, S. Soni, S.K. Sharma, M.C. Chattopadhyaya, Removal of tartrazine by activated carbon biosorbents of Lantana camara: Kinetics, equilibrium modeling and spectroscopic analysis. J. Environ. Chem. Eng. **3**, 79–88 (2015). https://doi.org/10.1016/j.jece.2014.11.026
45. S. Lagergren, About the theory of so-called adsorption of soluble substances. Kungliga Svenska Vetenskapsakademiens Handlingar **24**, 1–39 (1898)
46. S. Sharma, A. Hasan, N. Kumar, L.M. Pandey, Removal of methylene blue dye from aqueous solution using immobilized agrobacterium fabrum biomass along with iron oxide nanoparticles as biosorbent. Environ. Sci. Pollut. Control. Ser. **25**, 21605–21615 (2018). https://doi.org/10.1007/s11356-018-2280-z
47. G.J. Copelloa, A.M. Mebert, M. Raineri, M.P. Pesenti, L.E. Diaz, Removal of dyes from water using chitosan hydrogel/SiO_2 and chitin hydrogel/SiO_2 hybrid materials obtained by the sol–gel method. J. Hazard. Mater. **186**, 932–939 (2010). https://doi.org/10.1016/j.jhazmat.2010.11.097

Publisher's Note